Alloy Design Based on Computational Thermodynamics and Multi-objective Optimization: The Case of Medium-Mn Steels

JOHN S. ARISTEIDAKIS and GREGORY N. HAIDEMENOPOULOS

A new alloy design methodology is presented for the identification of alloy compositions, which exhibit process windows (PWs) satisfying specific design objectives and optimized for overall performance. The methodology is applied to the design of medium-Mn steels containing Al and/or Ni. By implementing computational alloy thermodynamics, a large composition space was investigated systematically to map the fraction and stability of retained austenite as a function of intercritical annealing temperature. Alloys exhibiting PWs, *i.e.*, an intercritical annealing range, which when applied satisfies the given design objectives, were identified. A multi-objective optimization method, involving Pareto optimality, was then applied to identify a list of optimum alloy compositions, which maximized retained austenite amount and stability, as well as intercritical annealing temperature, while minimized overall alloy content. A heuristic approach was finally employed in order to rank the optimum alloys. The methodology provided a final short list of alloy compositions and associated PWs ranked according to their overall performance. The proposed methodology could be the first step in the process of computational alloy design of medium-Mn steels or other alloy systems.

I. INTRODUCTION

MEDIUM-MN Steels containing 2 to 10 wt pct Mn, have received considerable attention as potential candidates for the third generation of advanced high-strength steels for use primarily in light-weight automotive applications. These steels aim to fill the gap between high-manganese twinning-induced plasticity steels and low-alloy transformation-induced plasticity steels. They were first introduced by Miller,[1] who focused his experiments on a 0.11C-5.7Mn steel with ultra-fine-grained microstructure. Excellent combinations of strength and elongation could be achieved by retained austenite stabilization through the partitioning of C and Mn by suitable thermomechanical treatment in the intercritical range. Since then, significant progress has been made as many researchers aim to further improve properties and processability in medium-Mn compositions. Although many and sometimes complex heat treatments have been proposed, the most widely used method of producing chemically and mechanically stabilized austenite is through intercritical annealing of either hot-rolled or cold-rolled material. Relevant publications are summarized in Table I, which depicts the alloy composition, annealing conditions, fraction of retained austenite, and associated mechanical properties.

The Mn content in this list varies between 3 and 11 wt pct while some recent studies have focused on the importance of Al, in concentrations up to 4 wt pct, as an effective way to increase annealing temperatures, inhibit cementite precipitation, and improve the overall retained austenite characteristics.[2] Recent advances in medium-Mn steels have been lately discussed.[12] The large variation in the Mn content and intercritical annealing conditions indicates that the development of this new class of steels is mostly based on empirical approaches. There have been limited attempts to systematically investigate the Fe-C-Mn-Ni-Al composition space and identify the effect of alloying elements and annealing conditions on the development of microstructure and associated mechanical properties. These limited efforts include the application of CALPHAD-based approaches to determine the effect of alloy composition[13] and the solute partitioning during intercritical annealing,[14] to select the optimum annealing temperature for a specific medium-Mn composition[3] and the tensile behavior during deformation of medium-Mn steels.[4] Kang *et al.*[13] studied computationally the effect of alloying on the equilibrium behavior of retained austenite in a Fe-C-Mn system, with the addition of Si, Al, or Cr. A similar model that also considers the effect of the austenite grain size and the martensitic transformation kinetics was employed by Lee and De Cooman,[3] in order to select a suitable annealing temperature for a Fe-0.3C-6Mn alloy. Kamoutsi *et al.*[14] modeled the kinetics of austenite formation during intercritical annealing in a Fe-C-Mn-Al system, with excellent agreement between theoretical and experimental findings. Rana *et al.*[4] combined thermodynamic equilibrium calculations for retained austenite prediction

JOHN S. ARISTEIDAKIS and GREGORY N. HAIDEMENOPOULOS are with the Laboratory of Materials, Department of Mechanical Engineering, University of Thessaly, Pedion Areos, 38500 Volos, Greece. Contact e-mail: hgreg@mie.uth.gr

Table I. Summary of Recent Activities in Medium-Mn Steels

Composition (Wt Pct)	Initial Condition	Annealing Temperature Range K (°C)	Annealing Time (min)	Retained Austenite (Pct)	Tensile Strength UTS (GPa)	Total Elongation ε_f (Pct)	Refs.
0.2C11Mn(2-4)Al	HR	873 (600) to 1173 (900) + tempering 473 (200)	60 + 20	8 to 83	0.75 to 1.45	19 to 40	2
0.3C6Mn	CR	873 (600) to 953 (680)	30 to 120	10 to 70	True UTS: 1.1 to 1.7	True ε_f: 2.5 to 30	3
0.1C7Mn0.13Si	CR	873 (600) to 923 (650)	10,080	31.8 to 44.3	0.85 to 1.2	12 to 38	4
0.11C5Mn	CR	923 (650)	1 to 720	5 to 22	0.7 to 0.9	18 to 40	5
0.2C(1.5-5)Mn1.5Si	HR	1073 (800) to 1173 (900) + tempering 453 (180) to 643 (370)	20 + 1.6 to 1667	7.9 to 8.3	1.27 to 1.6	13.8 to 14.6	6
0.07C7.9Mn0.14Si	HR	873 (600) to 973 (700)	30	7 to 39	1.5 to 1.65	15 to 28	7
0.18C11Mn3.8Al	CR	973 (700) to 1173 (900)	5	15 to 74	0.96 to 1.5	13 to 67	8
0.18C11Mn3.8Al	HR	973 (700) to 1173 (900) + tempering 473 (200)	60 + 20	8 to 71.9	0.88 to 1.1	35 to 40	9
0.17C(3-5)Mn1.5Al0.2Si0.2Mo (0-0.04)Nb	HR	673 (400)	5	6.4 to 17.7	0.98 to 1.3	—	10
0.16C6.5Mn1Al0.2Mo0.05Nb	CR	843 (570) to (690)	10 to 36	5 to 31	1.2	33	11

HR, hot rolled, *CR*, cold rolled, *UTS*, ultimate tensile strength, ε_f, total elongation.

with a strength model to determine the mechanical properties of medium-Mn steels containing 5 to 10 wt pct Mn, after intercritical annealing. The calculated tensile strength and uniform elongation matched very closely the experimental findings, proving that computational modeling is an essential tool which can accelerate significantly the alloy design process.

In the present study, the Fe-C-Mn-Al-Ni composition space for medium-Mn steels is investigated systematically. Ni is considered as an austenite stabilizer despite the associated increase in cost. However, it was decided to study the effect of Ni, considering that in the optimization stage, the reduction in total alloy content is taken into account. In the first stage, computational alloy thermodynamics, based on the CALPHAD approach, is applied in order to identify alloys exhibiting suitable process windows (PWs), which satisfy certain design objectives regarding the amount and stability of retained austenite. In the second stage, optimized alloys are identified with the application of multi-objective optimization methods. The methodology proposed is entirely based on equilibrium calculations and it is anticipated that a complementary study based on kinetic simulations and experimental validation should follow to complete the picture. However, at the present stage of development, the proposed alloy design process provides a short list of optimized alloys, which could serve as the starting point for a more detailed alloy development and evaluation in the laboratory scale, thus shortening the alloy development time considerably.

II. METHODOLOGY

A flow chart depicting the applied methodology is shown in Figure 1.

The alloy design process starts with the definition of the original composition space (OCS), the volume of which depends on the composition limits of the alloying elements. Suitable alloy design criteria are then defined in terms of the volume fraction of retained austenite, its stability, and the minimum width of the PW. Computational alloy thermodynamics is then employed in order to calculate suitable quantities such as the equilibrium austenite fraction and its composition as a function of annealing temperature. The application of the alloy design criteria to the OCS leads to the definition of a subspace, which contains the alloy compositions exhibiting a PW, *i.e.*, alloys, which satisfy the alloy design criteria. The next step is to perform a multi-objective optimization process in order to identify the Pareto optimal solutions and then rank the selected alloys according to a suitable heuristic method. The optimization process leads to the definition of a short list of optimized alloy compositions. The methodology is presented in detail in the following sections.

A. *Definition of the Original Composition Space*

The range of alloy compositions in C, Mn, Al, and Ni, which defines the OCS is given in Table II. The
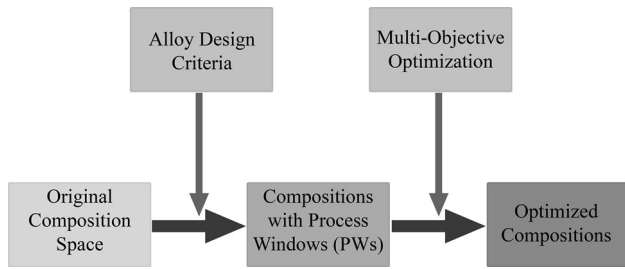
Fig. 1—Flow chart of the applied methodology for alloy design.

Table II. Range of Alloy Compositions Defining the Original Composition Space

	Lower Limit	Upper Limit	Increment
Temperature	673 K (400 °C)	1273 K (1000 °C)	2 K (°C)
C (wt pct)	0.1	0.3	0.05
Mn (wt pct)	2	10	1
Ni (wt pct)	0	3	0.5
Al (wt pct)	0	4	0.5
Si (wt pct)	0.15 (constant)		
Fe	balance		
Total number of alloys	2835		

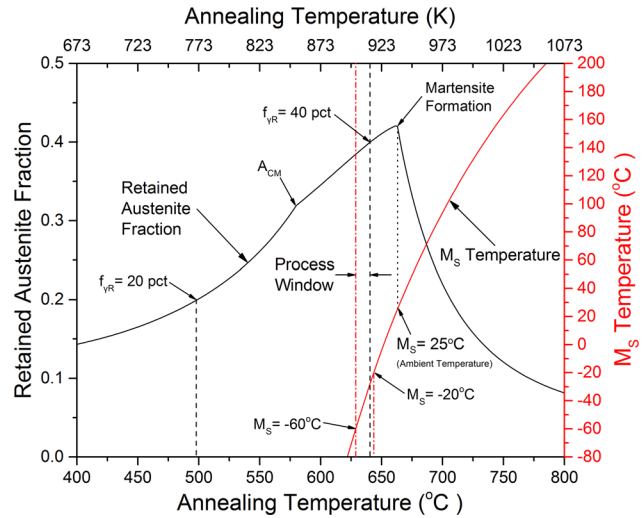

Fig. 2—Retained Austenite Fraction and M_S Temperature as a function of annealing temperature for a Fe-0.1C-9Mn-2Ni-4Al (wt pct) alloy. A Process Window as defined in Table III is apparent.

annealing temperature range was considered 673 K to 1273 K (400 °C to 1000 °C). Based on the limits and the increment, the total number of alloys in the OCS is 2835.

B. Alloy Design Criteria and Process Windows

The alloy design criteria are a set of parameters specifying the desirable microstructure. The parameters chosen in this work are the fraction of retained austenite, the stability of austenite, and the range of the intercritical annealing temperature (PW width). An additional requirement is that cementite should not form during intercritical annealing to allow sufficient C partitioning to the austenite for stabilization. The criteria are shown in Table III. The fraction of retained austenite $f_{\gamma R}$ is set between 20 and 40 pct, as it has been suggested that this range exhibits good combinations of strength and ductility in certain medium-Mn steels.[15] The stability of austenite, is characterized by the M_S temperature, in the range 253 K to 213 K (−20 °C to −60 °C). A PW is then defined as the annealing temperature range, which allows the formation of the specified amount of austenite with specified M_S temperature, without the presence of cementite. Additionally, the width of a PW should be at least 10 °C, so that the heat treatment can be specified industrially.

An example of an alloy exhibiting a PW is shown in Figure 2. It has a composition of Fe-0.1C-9Mn-2Ni-4Al (wt pct). The fraction of retained austenite and its associated M_S temperature are plotted as a function of the intercritical annealing temperature. The specific thermodynamic calculations are described in Section II–C. The fraction of retained austenite reaches a peak at 943 K (670 °C) since the austenite forming above this temperature has an M_S temperature above room temperature and transforms partially to martensite. A_{CM} is the temperature above which there is no cementite formation during intercritical annealing. The application of the design criteria of Table III defines a PW between 902 K (629 °C) and 912 K (639 °C). If the alloy is intercritically annealed in the specified PW, then all design criteria of Table III will be satisfied.

An alloy which does not exhibit a PW is shown in Figure 3. It has a composition Fe-0.15C-8Mn (wt pct) and does not contain either Ni or Al. As depicted in the figure, the intercritical annealing range satisfying the fraction of retained austenite and M_S temperature as set in Table III is below the A_{CM} temperature. Therefore, this alloy does not exhibit a suitable PW, to satisfy all the design criteria of Table III.

C. Thermodynamic Calculations

Thermodynamic calculations were performed for each one of the 2835 different alloys in the OCS, using the CALPHAD approach,[16] implemented through the

Table III. Alloy Design Criteria Used to Identify Process Windows

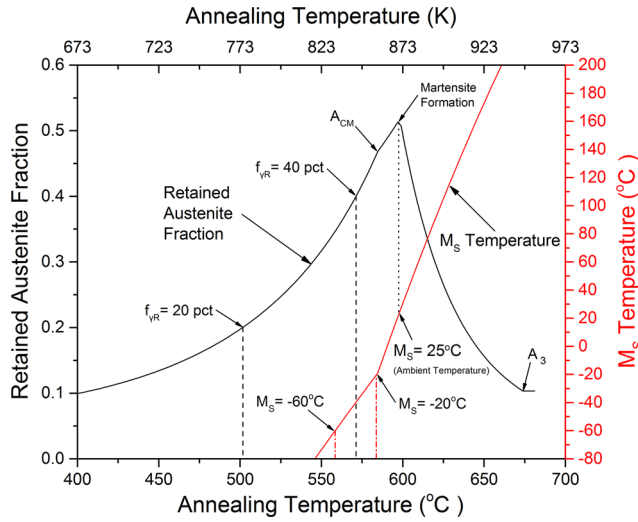| Basic PW Requirements	Retained Austenite No Cementite
Retained austenite fraction	$20 \leq f_{\gamma R}(T) \leq 40$ pct
Retained austenite stability	213 K (−60 °C) $\leq M_S(T) \leq$ 253 K (−20 °C)
PW width	$\Delta T = T_{Max} - T_{Min} \geq 10$ K (−20 °C)

Fig. 3—Retained Austenite Fraction and M_S Temperature as a function of annealing temperature for a Fe-0.15C-8Mn (wt pct) alloy. The Process Window conditions, defined in Table III, are not satisfied, and thus the alloy does not exhibit a PW.

Thermo-Calc software.[17] More specifically, the TCFE6 Database of Thermo-Calc was used to calculate the volume fraction of phases at equilibrium, as well as the corresponding chemical compositions as a function of intercritical annealing temperature, in the range of 673 K to 1273 K (400 °C to 1000 °C). Due to the large number of calculations required, a custom Thermo-Calc interface was created. The interface operates on Thermo-Calc and enables calculations to be carried out automatically. The raw data produced by Thermo-Calc were processed to determine the fraction of retained austenite and its stability, as a function of annealing temperature. The M_S temperature was used as a measure of austenite stability in this work. The M_S temperature is given by Andrews[18] as a function of the equilibrium austenite composition as

$$M_S(T) = 539 - 423W_C - 30.4W_{Mn} - 7.5W_{Si}$$
$$- 17.7W_{Ni} + 30W_{Al} \; (°C), \qquad [1]$$

where W_C, W_{Mn}, W_{Si}, W_{Ni}, and W_{Al} are the alloying contents of austenite in wt pct for each annealing temperature T. The fraction $f_m(T)$ of the austenite transformed into martensite can be approximated by the Koistinen–Marburger model[19] as follows:

$$f_m(T) = 1 - \exp[-0.011(M_S(T) - T_R)], \qquad [2]$$

where T_R is the ambient temperature (298 K or 25 °C). Then the volume fraction of the retained austenite is given by subtracting the volume fraction of the martensite formed from that of the equilibrium austenite

$$f_{\gamma R}(T) = f_\gamma(T)(1 - f_m(T)). \qquad [3]$$

As mentioned above, a PW, is an annealing temperature range, which satisfies the alloy design criteria of Table III. Once a PW is identified, a set of five PW attributes are calculated. The maximum and minimum annealing temperatures, T_{Min} and T_{Max} defining the PW and the reference temperature T_{Ref}, which is defined as $T_{Ref} = T_{Min} + 3/4\Delta T$. In addition, the retained austenite volume fraction and the M_S are calculated at T_{Ref}. The five attributes characterize a PW and along with the nominal chemical composition, are used during the optimization stage described below.

D. Multi-objective Optimization

The scope of the optimization process is to identify a short list of alloys, from those found to exhibit a PW. The methodology proposed combines features of classical multi-component optimization techniques with heuristic decision-making approaches to determine which alloys are the best candidates for the specific application. The decision variable is a vector composed of the nominal C, Mn, Ni, and Al compositions, which is constrained inside the region of the OCS found to exhibit PWs. The selected design objectives are the volume fraction of retained austenite and the M_S temperature, calculated for each alloy at the reference annealing temperature T_{Ref}. In addition, a new parameter, termed the composition index CI, discussed in detail in Section II–E, is introduced to account for the total alloying content of each alloy. The CI is used to favor alloys with less C and Mn and thus to improve weldability and to reduce raw material cost. It should be noted that CI as well as $f_{\gamma R}$ are dimensionless, whereas T_{Ref} and M_S are expressed in degrees Celsius. Optimal compositions should maximize retained austenite and annealing temperature, while minimizing the M_S temperature and CI as expressed by

$$\text{Maximize: } \{f_{\gamma R}(T_{Ref}), \; T_{Ref}\},$$
$$\text{Minimize: } \{M_S(T_{Ref}), \; CI\}. \qquad [4]$$

Because there are multiple alloy design criteria, a single optimum solution might not be feasible, since the improvement of one index might cause the deterioration of the other ones. Instead, there is usually a tradeoff between the objectives, so many optimal compositions can be identified, depending on the relevant importance of each individual alloy design objective. Then the problem can be modeled as a multi-objective optimization problem (MOOP). In the context of MOOP, an alloy composition can be considered optimal if it results in objectives that lay on the Pareto front.[20,21] A formal definition of the Pareto optimality, is the subset of solutions, for which it is not possible to improve an objective without simultaneously worsening at least one of the others. Assuming that $F(x) = [f_1(x), f_2(x),...,f_k(x)]^T$ is a vector of k objective functions and $x \in \Omega$ is the decision vector, bounded in a region Ω which is a subset of $\mathbb{R}^n$, then a formal mathematical definition of Pareto optimality can be given. For a maximization problem, a certain decision vector x^*, is thought to be a Pareto optimal solution if no other acceptable decision vector x can be found so that $f_i(x) \geq f_i(x^*)$ for every integer i from 1 to k and $f_i(x) > f_i(x^*)$ for at least one i. Then the Pareto front is

defined as the set of points on the objective function space that correspond to every Pareto optimal solution.

The optimization is carried out in a discrete composition space containing the alloy compositions exhibiting a PW. No additional constraints regarding the design objectives are needed, since they have already been applied to identify the suitable compositions. To formulate the process as a discrete multi-objective maximization problem, an objective vector J is created, which is composed of the four individual objective functions.

$$\text{Maximize: } J = \begin{bmatrix} J_1 & J_2 & J_3 & J_4 \end{bmatrix}^T, \qquad [5]$$

where

$$J_1 = f_{\gamma R}(T_{\text{Ref}}), \quad J_2 = T_{\text{Ref}}, \quad J_3 = -M_S(T_{\text{Ref}}), J_4 = -\text{CI}. \qquad [6]$$

The first two components J_1 and J_2 of J are the retained austenite fraction and the reference annealing temperature, respectively, whereas J_3 and J_4 correspond to the stability and composition objectives multiplied by -1 so that all components need to be maximized simultaneously. Since the elements of the objective vector are expressed in different scales and units, it is important to normalize J with an appropriate quantity.[22] For that purpose, two vectors J_{Max} and J_{Min} composed of the maximum and minimum values of each individual objective J_i, are computed

$$J_{Max} = \begin{bmatrix} \text{Max}(J_1) & \text{Max}(J_2) & \text{Max}(J_3) & \text{Max}(J_4) \end{bmatrix}^T, \qquad [7]$$

$$J_{Min} = \begin{bmatrix} \text{Min}(J_1) & \text{Min}(J_2) & \text{Min}(J_3) & \text{Min}(J_4) \end{bmatrix}^T. \qquad [8]$$

Then the normalized objective vector J_N with elements J_{N_i} is calculated

$$J_{N_i} = \frac{J_i - J_{\text{Min}_i}}{J_{\text{Max}_i} - J_{\text{Min}_i}}, \quad \forall i \in \{1, 2, 3, 4\}, \qquad [9]$$

so that $0 \leq J_{N_i} \leq 1 \ \forall i \in \{1, 2, 3, 4\}$.

Pareto optimal solutions are identified by exhaustively examining all compositions found to exhibit a PW. This has been accomplished using the formal Pareto optimality definition. In this case, $F(x) = J_N$ and x is the decision vector, i.e., a vector composed of the chemical composition bounded in the region of the OCS that supports PWs. The set of Pareto optimal solutions might be very extensive and although each member is optimal in a sense, a method is needed to select a short list of solutions with overall better performance. To rank the Pareto optimal solutions, a heuristic approach is employed based on a function that aggregates the four objectives into a single parameter. The geometric mean (GM) of the normalized objective vector components J_{N_i}

$$\text{GM} = \left(\prod_{i=1}^{4} J_{N_i} \right)^{\frac{1}{4}} = \sqrt[4]{J_{N_1} J_{N_2} J_{N_3} J_{N_4}}, \qquad [10]$$

calculated for each Pareto optimal solution, was chosen as the aggregation function, so that solutions with higher GM rating are thought to have the best overall performance with respect to the design objectives. The idea behind GM is that unlike the arithmetic mean or other heuristic indices, GM takes large values only if all four objectives are large. As a result, compositions that perform excellently in two or three objectives and poorly in the others are ranked lower than those with consistently large but not extreme objective values. The ten Pareto optimal compositions with the highest GM values are the final result of the optimization process and form the short list of alloys with optimized properties.

The components J_1, J_2, and J_3 of the objective vector J are known quantities, since they were calculated at an earlier stage for each composition. In contrast, the component J_4, which corresponds to the CI, is a function of the nominal chemical composition and should be evaluated for the corresponding alloys which exhibit PWs, prior to optimization. These calculations are discussed in the next section.

E. Composition Index Analysis

The CI comprises the alloying contents of a certain nominal composition through a weighted sum.[22,23] Since it is not required during the PW selection process, CI is only evaluated in alloys found to exhibit PWs. To compute CI for a specific alloy, first a composition vector C is created, composed of the alloy's C, Mn, Ni, and Al contents.

$$C = \begin{bmatrix} C_1 & C_2 & C_3 & C_4 \end{bmatrix}^T, \qquad [11]$$

where:

$$\begin{array}{ll} C_1 = \text{C wt pct}, & C_2 = \text{Mn wt pct}, \\ C_3 = \text{Ni wt pct}, & C_4 = \text{Al wt pct}. \end{array} \qquad [12]$$

Then the vectors C_{Max} and C_{Min} are calculated by finding the maximum and minimum content values expressed in alloys that exhibit a PW

$$C_{Max} = \begin{bmatrix} \text{Max}(C_1) & \text{Max}(C_2) & \text{Max}(C_3) & \text{Max}(C_4) \end{bmatrix}^T, \qquad [13]$$

$$C_{Min} = \begin{bmatrix} \text{Min}(C_1) & \text{Min}(C_2) & \text{Min}(C_3) & \text{Min}(C_4) \end{bmatrix}^T. \qquad [14]$$

In accordance to the normalization method used for J_N, C_{Max} and C_{Min} are used to normalize C and to create the normalized composition vector C_N with elements C_{N_i}

$$C_{N_i} = \frac{C_i - C_{\text{Min}_i}}{C_{\text{Max}_i} - C_{\text{Min}_i}}, \quad \forall i \in \{1, 2, 3, 4\}, \qquad [15]$$

so that $0 \leq C_{N_i} \leq 1 \ \forall i \in \{1, 2, 3, 4\}$.

The CI is defined as the dot product of a composition weight vector W_C with the normalized alloying contents C_N. In other words, CI is a weighted sum of the normalized nominal alloying concentrations, as

$$CI = \boldsymbol{W}_C \cdot C_N = \sum_{i=1}^{4} w_{c_i} C_{N_i}, \qquad [16]$$

where

$$\boldsymbol{W}_C = \begin{bmatrix} w_{c_1} & w_{c_2} & w_{c_3} & w_{c_4} \end{bmatrix} \quad \text{and} \quad \sum_{i=1}^{4} w_{c_i} = 1. \quad [17]$$

The composition weight vector $\boldsymbol{W}_C$ remains constant throughout the process and should be selected carefully, since it directly determines which elements are favored and which are not. The vector should always be non-negative and the sum of its elements should add up to unity.

Although the selection of appropriate weights is entirely empirical, the process can be standardized, to a certain extent, with the application of the analytical hierarchy process (AHP).[24] This method allows the quantification of the relative importance of the different elements. Since the elements of interest are four, the first step of the process is to create a square 4×4 pairwise comparison matrix $\boldsymbol{P}$. The values p_{ij} of $\boldsymbol{P}$ are then determined by the relative importance of component i in comparison to component j in terms of some penalty (cost, weldability). Additionally, the product of each element p_{ij} with its symmetric element p_{ji} must always equal to one

$$p_{ij}p_{ji} = 1 \Leftrightarrow p_{ji} = \frac{1}{p_{ij}}, \quad \forall i, j \in \{1, 2, 3, 4\}. \quad [18]$$

As a consequence, the diagonal terms p_{ii} are equal to one and elements above and below the diagonal are inversely proportional. Assuming that index i is more important than index j, then the relative importance p_{ij} is ranked according to a scale ranging from 1 to 9, where 1 indicates no hierarchical difference and 9 an extreme significance of element i over j. In this application, the relative importance provides an indication of how negative influence an alloying element has compared to another. The pairwise comparison matrix used in this study is given in Table IV. As an example, the elements $p_{13} = 5$ and $p_{21} = 3$ of matrix $\boldsymbol{P}$, indicate that C has a strong negative influence compared to Al and Mn has a moderate negative influence compared to C. Then the symmetric elements p_{31} and p_{12} must take the value $p_{12} = 1/3$ and $p_{13} = 1/5$ so that $p_{12}p_{21} = p_{13}p_{31} = 1$.

The next step is to normalize $\boldsymbol{P}$ by dividing its elements with the sum of the corresponding column

$$\overline{np}_{ij} = \frac{p_{ij}}{\sum_{k=1}^{4} p_{kj}}. \qquad [19]$$

With this operation, a 4×4 normalized pairwise comparison matrix $\mathbf{NP}$ is constructed, with elements $\overline{np}_{ij}$. Finally, the appropriate CI weights (w_{c_i}) are given by computing the mean value of each row of $\mathbf{NP}$

$$w_{c_i} = \frac{\sum_{k=1}^{4} \overline{np}_{ik}}{4}. \qquad [20]$$

As the pairwise comparison matrix is assigned with values, a few inconsistent ratings might appear, which could impede the validity of the calculated weight vector. The AHP method provides a systematic approach in order to estimate the consistency of $\boldsymbol{P}$, with the use of a parameter named consistency rate (CR). CR is defined as the consistency index (C_nI) of $\boldsymbol{P}$ over RI, which is the consistency index of a random pairwise comparison matrix.[25,26] Then the CR can be calculated with the following set of equations

$$CR = \frac{C_nI}{RI}, \qquad [21a]$$

$$C_nI = \frac{\lambda - n}{n - 1}, \qquad [21b]$$

where

$$\lambda = \sum_{i=1}^{n} \sum_{j=1}^{n} p_{ij}w_{c_j}, \qquad [21c]$$

and n is the number of rows or columns of $\mathbf{NP}$. In the current application, $n = 4$. The value of RI can be approximated by

$$RI = \frac{1.95(n - 2)}{n}. \qquad [21d]$$

The inconsistency level of the matrix $\boldsymbol{P}$ is thought to be acceptable when $CR \leq 0.1$.[25,26] The values of $\boldsymbol{P}$ might need to be revised in the case that CR greatly exceeds the limit value.

For the pairwise comparison matrix illustrated in Table IV, the computed weight vector is

$$\boldsymbol{W}_C = \begin{bmatrix} 0.259 & 0.568 & 0.119 & 0.054 \end{bmatrix}.$$

The sum of the individual CI weights is unity and the consistency analysis described above reveals that the weights are valid since the CR is $CR = 0.048$ which is well below the acceptable limit. It can be observed that this specific set of weights causes CI to take large values in alloys with high Mn and C content. As $J_4 = -CI$ is maximized, compositions with lower C and Mn are favored, which should improve weldability and reduce raw material cost. The weights that correspond to Ni and Al are significantly lower than those of C and Mn. This indicates that higher Ni and Al compositions are

Table IV. Pairwise Comparison Matrix P

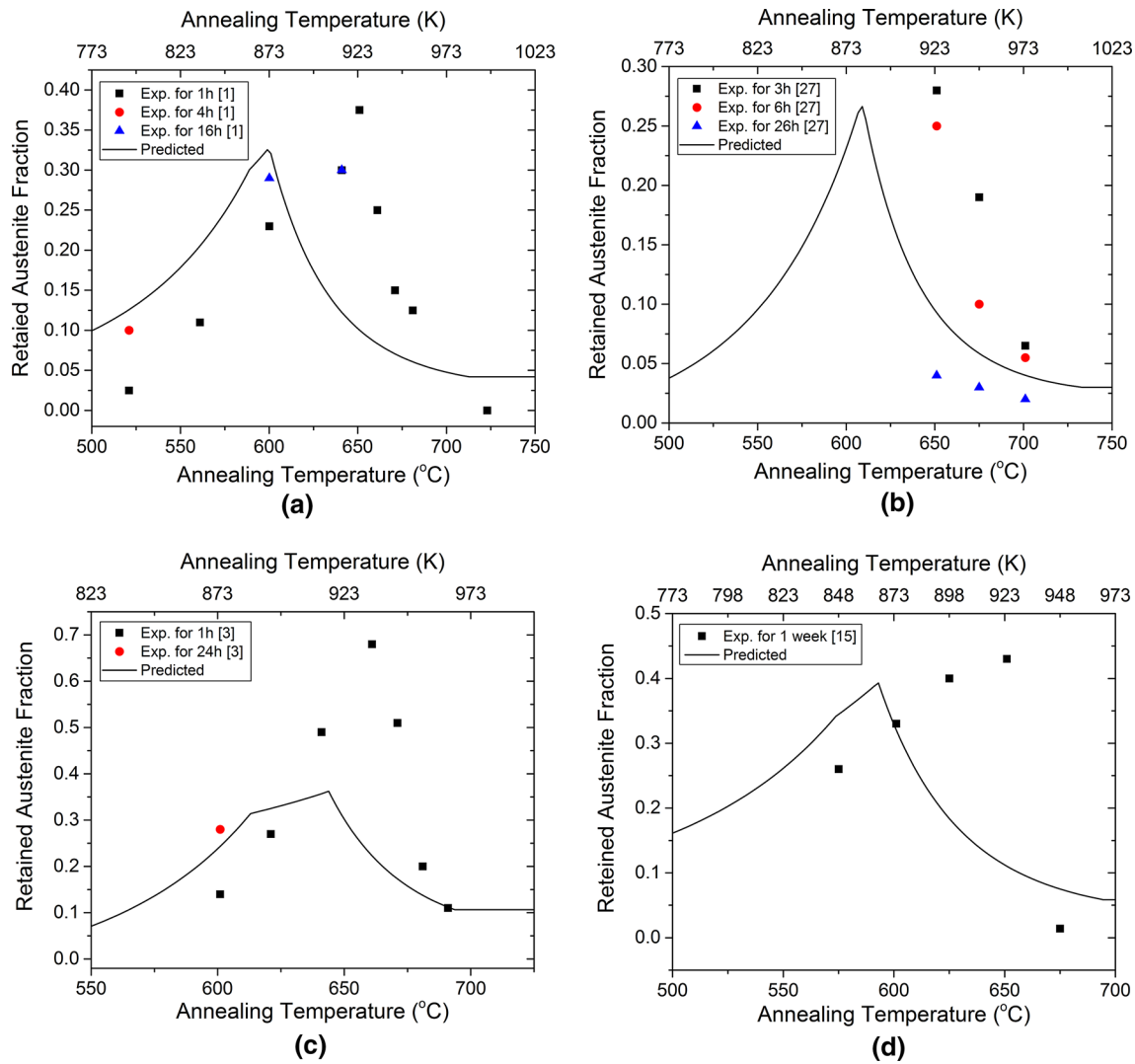|	C	Mn	Ni	Al
C	1	1/3	3	5
Mn	3	1	5	8
Ni	1/3	1/5	1	3
Al	1/5	1/8	1/3	1

Fig. 4—Retained austenite fractions as measured by (a) Miller et al.[1] for a 0.11C5.7Mn steel, (b) Huang et al.[27] for a 0.1C5.1Mn steel, (c) Lee and De Cooman[3] for a 0.3C6Mn steel and (d) Gibbs et al.[15] for a 0.1C7.1Mn steel. The solid line represents the predicted equilibrium results for the same alloys.

tolerated. Ni could also potentially increase the production cost, however, since the maximum amount cannot exceed 3 pct by weight the effect is negligible. In contrast, recent studies[2] have shown that Al benefits the overall performance of medium-Mn steels, and thus high Al compositions are not penalized with an increased CI value.

III. RESULTS AND DISCUSSION

A. Experimental Validation

To assess the validity of the proposed model, the predicted retained austenite fractions, as a function of annealing temperature, were compared with published experimental results. Comparison between model predictions and experimental results from Miller[1] for a 0.11C5.7Mn steel intercritically annealed for 1, 4, and 16 hours at temperatures ranging between 793 K (520 °C) and 993 K (720 °C) are depicted in

Figure 4(a). Comparison with experimental results from Huang et al.[27] for a 0.1C5.1Mn steel, after intercritical annealing at 923 K (650 °C), 948 K (675 °C), and 973 K (700 °C) for 3, 6, and 26 hours are presented in Figure 4(b). Comparison with results from Lee and De Cooman[3] for a 0.3C6Mn steel, annealed at temperatures between 873 K (600 °C) and 963 K (690 °C) for 1 and 24 hours, are depicted in Figure 4(c). Finally, comparison with results from Gibbs et al.[15] for a 0.1C7.1Mn steel after intercritical annealing for 1 week, at temperatures ranging between 848 K (575 °C) and 948 K (675 °C), are presented in Figure 4(d). In all cases, deviations between experimental and predicted austenite fractions could be attributed to the fact that the model is entirely based on thermodynamic equilibrium calculations, and in most cases, equilibrium has not been established during laboratory annealing cycles. However, the comparison indicates that the model approaches the experimental values for long annealing times. In addition, the general variation of austenite
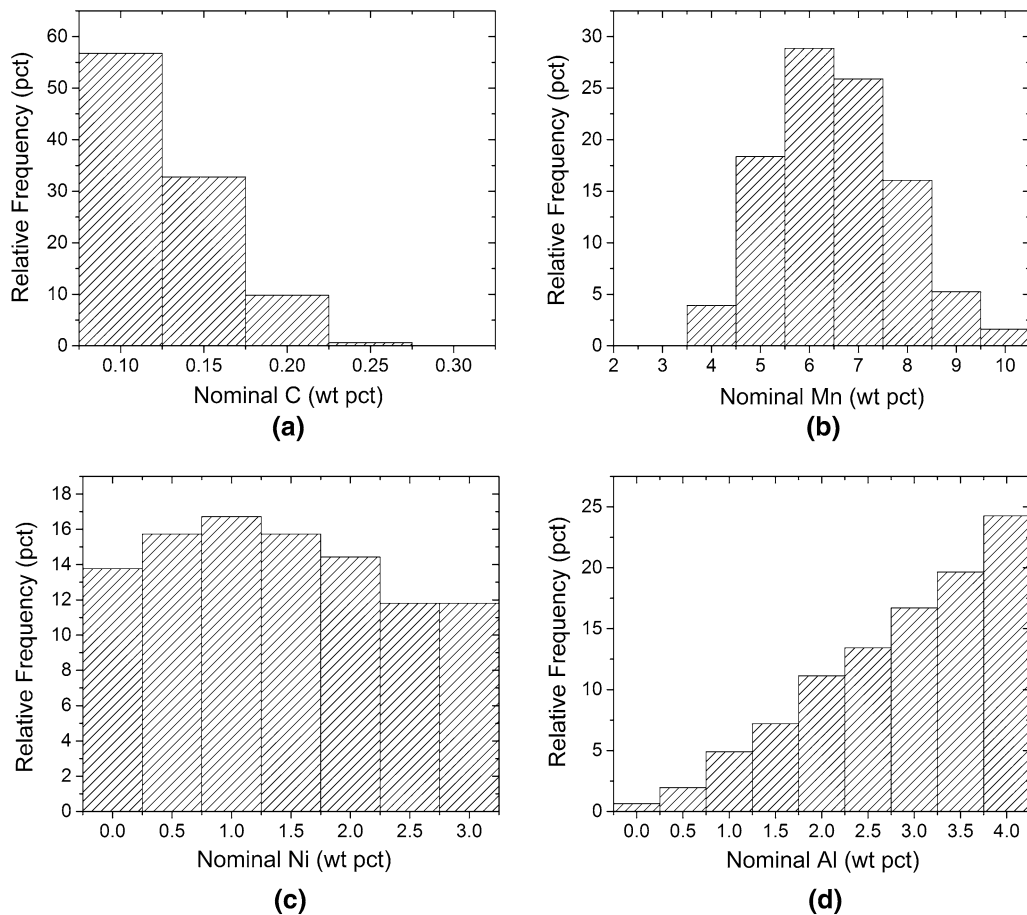
Fig. 5—Distribution of PWs found in alloys with a specific amount of (*a*) Carbon, (*b*) Manganese, (*c*) Nickel, and (*d*) Aluminum.

fraction with annealing temperature is predicted by the model, providing confidence that the methodology described here could be used as a first step of the alloy design process. As discussed in Section III–G below, kinetic calculations, involving the annealing times, are planned to be performed for the short list of the alloys investigated in the present study.

B. *Description of Alloys Exhibiting Process Windows*

Using the methodology described above, from a total of 2835 alloys comprising the OCS, only 305 were identified to satisfy all alloy design criteria. This corresponds to approximately 11 pct of the total compositions. It should be noted that the number of acceptable compositions, is strongly linked to the set constraints, since a small change in the restrictions, might result in significantly different results.

The effect of nominal chemical composition on the number of alloys that exhibit a PW is depicted in Figure 5. More specifically, Figure 5(a) illustrates the effect of C. Over 85 pct of the identified PWs contain no more than 0.15 pct C. The population drastically decreases as C concentration rises, until a critical value of 0.3 pct is reached, where no PWs are identified. On the other hand, the distribution of PWs with respect to Mn content approximates a normal distribution with a

mode value of 6 pct, as illustrated in Figure 5(b). Over 90 pct of the population contains between 5 and 8 pct Mn by weight, whereas no suitable alloys were found to contain less than 4 pct Mn. Similarly, very few alloys contain 10 pct Mn, as the number of PWs rapidly decays when Mn exceeds 8 pct. Unlike C and Mn, Ni concentration seems to leave unaffected the number of PWs. As indicated in Figure 5(c), Ni distribution is very uniform with almost identical probability of finding a PW regardless of Ni content. Although the effect might be neglected, a slightly higher number of alloys with 1 pct Ni are identified. Finally, the effect of Al is shown in Figure 5(d). The distribution indicates a clear uphill trend, since the number of PWs increases almost linearly with the addition of Al. Following the observed trends, it is safe to assume that increasing the OCS toward higher Al and Ni contents could reveal more alloys that exhibit a PW. Increasing the carbon or manganese content alone, above the maximum current values does not seem to identify additional PWs.

Although the histograms of Figure 5 can give a general qualitative overview of what compositions seem to favor PWs, they cannot provide specific information about possible interactions among the different elements. Since the OCS is four dimensional, visualizing the alloys that exhibit a PW is not trivial. Two complementary methods of achieving that are proposed.
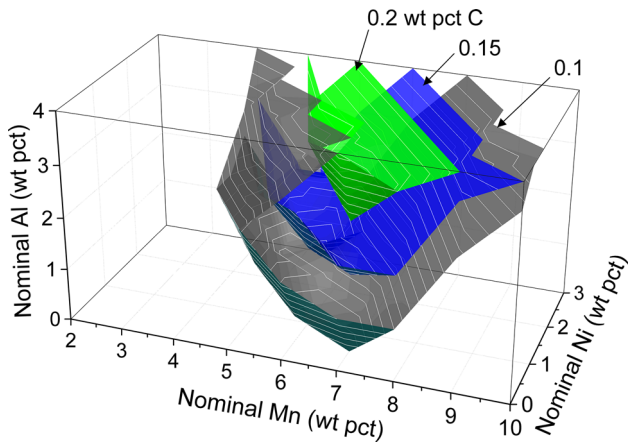
Fig. 6—Three-Dimensional Carbon Contours illustrating the regions of the original composition space found to exhibit PWs.

In the first method, the three-dimensional contours of the four-dimensional space at different carbon intervals define a set of volumes in the Mn-Ni-Al composition subspace. Plotting the boundary surfaces instead of the solid C contour volumes is preferred because it allows for hidden details to emerge, as shown in Figures 6, 7(a), 8(a), and 9(a). Every alloy lying inside the contour volume, exhibits a PW. In the second visualization method, the thickness of each C contour volume is projected onto each two-dimensional composition plane. The number of PWs identified is depicted in Figures 7(b), 8(b), and 9(b), as projected on the Mn-Ni plane, for different carbon contents. Similarly, Figures 7(c), 8(c), 9(c) and 7(d), 8(d), 9(d) depict the corresponding plots on the Mn-Al and Ni-Al planes, respectively.

As indicated by Figure 6, the carbon content has a profound effect on the morphology and topology of the projected volume. The majority of PWs identified are located at low C concentrations, and thus the volume is larger. As C increases, the volume shrinks significantly and when it reaches a critical value of 0.25 pct, a boundary surface can no longer be defined, since there are only two alloys that exhibit a PW. Although carbon content affects significantly the number of PWs, it does not seem to influence the general morphology of the boundary surfaces. The contour volume tends to shift upward to higher Al concentrations, without changing the shape significantly. The effect is particularly visible in Figure 6, as well as in Figures 7, 8, and 9. As depicted in the corresponding density plots of Figures 7, 8, and 9, the maximum density spots remain in roughly the same location on the Mn-Ni planes and move to higher Al concentrations on the Mn-Al and Ni-Al planes. A direct consequence of this behavior is that in order to identify PWs in high carbon alloys, the addition of large amounts of aluminum is necessary. This phenomenon is mostly attributed to the fact that increased C content favors cementite precipitation in the intercritical range and since no cementite is desired, the number of PWs drops. In contrast, the addition of aluminum suppresses carbide formation and thus PWs can be identified.

1. *Alloys with 0.1 pct C*

The 0.1 pct carbon three-dimensional contour, shown in Figure 7(a), includes the majority of PWs identified in the examined OCS. The volume spans a large portion of the OCS, ranging from 4 to 10 pct Mn, 0 to 3 pct Ni, and 0 to 4 pct Al while remaining partially unbounded at 4 pct Al, 10 pct Mn, and 3 pct Ni. This is a strong indication that PWs continue to exist outside the OCS. Particularly in the case of Al, it seems that an increase above 4 pct could reveal more PWs. From the orientation of the boundary surfaces, as well as the density projection on the Mn-Ni plane, it is evident that there is an almost linear correlation between Mn and Ni. The effect is apparent on the lower boundary surface, which forms a V-shaped channel following a linear path dividing the volume into a high and a low Mn-Ni section. Addition of Ni appears to reduce the amount of Mn required to identify a PW, provided that the Al content is sufficient. So PWs can be identified at Mn contents as low as 4 pct, which would be impossible without the addition of Ni. However, excess Ni can also rule out alloys, particularly those with Mn content over 8 pct. PWs in these alloys could be identified by increasing the Al content over 4 pct, outside the OCS. As shown in Figures 7(a) and (c), as the Al content increases, PWs in the high Mn-Ni region are identified. In fact, the boundary surface in that region resembles a tilted flat plane, indicating a linear relation between Mn and Al as well. In contrast, the boundary surface of the low Mn-Ni region is significantly curved on both the Mn-Ni and Mn-Al planes. Initially as the Al content is increased, alloys with low Mn and Ni content exhibit PWs, and the projected volume increases until a critical value of 2 pct Al is reached. From that point on, further addition of Al inhibits PW identification. On the Ni-Al plane, illustrated in Figure 7(d), almost each combination of Al and Ni examined, exhibits a PW provided that the right amount of Mn is added. For Al above 2 pct, which corresponds to the transition point of the low Mn-Ni boundary surface, the density becomes fairly uniform as the two boundary surfaces are almost parallel to each other. The compositions that seem to better facilitate PWs can be identified as the high-density regions in the corresponding density diagrams. For alloys containing 0.1 pct C, more PWs were identified in the 6 to 8 pct Mn, 0.5 to 1.5 pct Ni, and 1 to 4 pct Al region. As a general outline, although at low Mn contents, the addition of Ni and Al to a specific range, promotes PWs, at high Mn alloys excess Ni inhibits them. So as the Mn content increases, Al should be increased and Ni decreased, in order to stay inside the contour volume. The overall morphology of the boundary surface indicates that the entire volume has not been revealed and an extension of the OCS could be considered, especially in the direction of the Al.

2. *Alloys with 0.15 pct C*

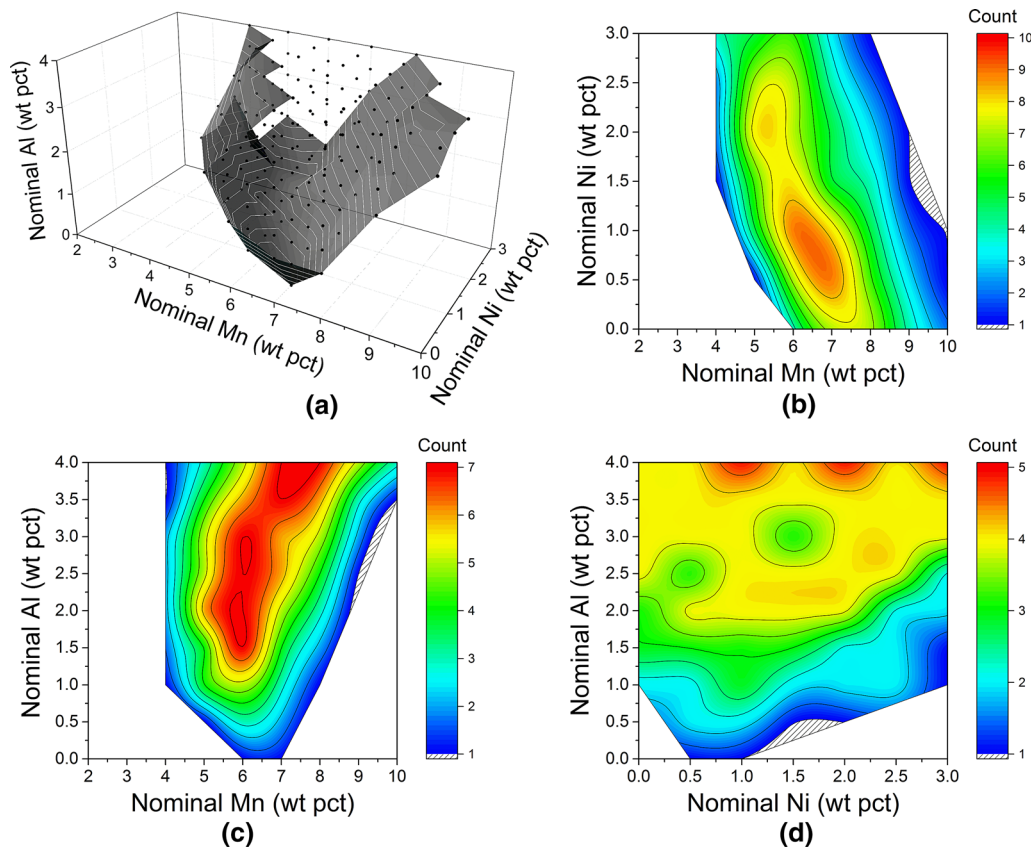The behavior of alloys with 0.15 pct C is very similar to those with 0.1 pct C. The main difference is that the

Fig. 7—0.10 Pct C: (*a*) 3D Contour, (*b*) Mn-Ni Projection, (*c*) Mn-Al Projection, and (*d*) Ni-Al Projection.

contour volume is shifted to higher Al contents, as shown in Figure 8(a). The Mn and Ni contents that favor PWs are the same; however, Al cannot drop below 1 pct by weight. The linearity between Mn and Ni as well as Mn and Al is still present. and thus the volume can be divided to a high and a low Mn-Ni section. The boundary surface once again forms a characteristic V-shape with a relatively flat high Mn-Ni region boundary. In contrast, the border surface on the low Mn-Ni region remains curved, however, it is abrupted when Al reaches 2 pct. As the Al content increases further, the boundary remains perpendicular to the Mn-Ni plane. For the sake of simplicity, the vertical surface is not depicted in Figure 8(a). Due to the volume shift, local and global minima are located at higher Al contents. Considering the density plots in Figures 8(b) through and (d), it is evident that the composition range that exhibits PWs, has shrunk significantly with the addition of more carbon, especially in the direction of Mn and Al. The effect of Ni remains unchanged since PWs can still be identified at each increment. Although small discrepancies are noticeable, the density distributions are very similar to that of 0.1 pct C. The high-density spot has moved to slightly lower Mn and higher Ni contents on the Mn-Ni projection, whereas it has been confined to a small region of 5 to 7 pct Mn and 3.5 to 4 pct Al on the Mn-Al plane. On the other hand, the densest area on the Ni-Al diagram still lies on a narrow zone located at 4 pct Al.

3. Alloys with 0.2 pct C

The trends observed at 0.15 wt pct C are still found at the 0.2 wt pct C contours. As seen in Figure 9(a), the composition range that exhibits PWs has shrunk even further, mostly in the Al direction. Considering the corresponding density plots in Figures 9(b) through (d), it can be seen that in order to identify PWs, the addition of at least 2.5 wt pct Al is required, so that cementite precipitation is inhibited. In accordance with the 0.15 pct C contours, the Mn range becomes narrower and the Ni range remains unaffected. Although the linear relation between Mn and Ni is still present, the volume shrinks to the point where the linear correlation of Mn and Al can no longer be observed. On the Mn-Al plane, the densest spot remains located in the same region of 6 to 7 pct Mn and 4 pct Al. In contrast, the majority of PWs on the Mn-Ni plane are now found in an area of 7 to 8 pct Mn and only 0.5 pct Ni. An increase of the carbon content requires lower Ni and higher Al, so that PWs are identified.

4. Alloys with 0.25 pct C

When the C content reaches 0.25 wt pct, a volume can no longer be defined since only two compositions exhibit a PW. As shown in Figure 10, the first alloy contains 8 pct Mn and no Ni, whereas the second has a lower Mn content at 7 pct but contains 1 pct Ni. Both alloys contain 4 pct Al, which seems to be an important limiting factor in PW identification. A further increase
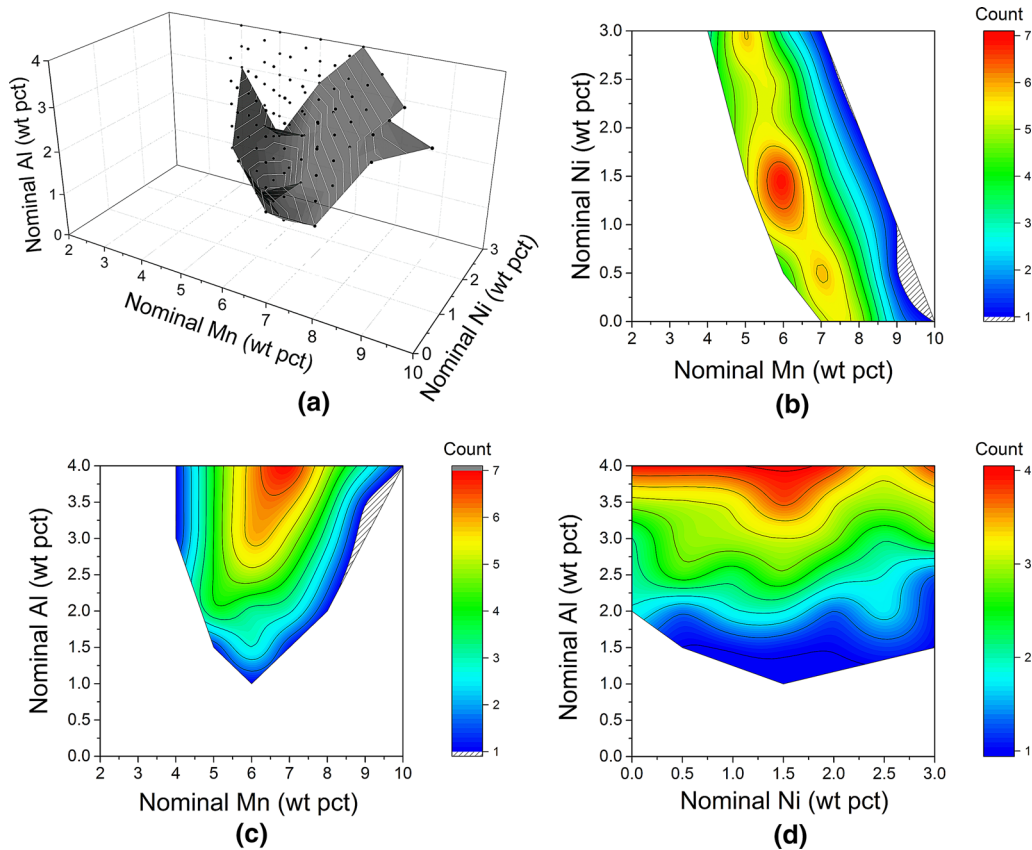
Fig. 8—0.15 Pct C: (*a*) 3D Contour, (*b*) Mn-Ni Projection, (*c*) Mn-Al Projection, and (*d*) Ni-Al Projection.

in carbon beyond 0.25 pct results in a complete absence of PWs inside the mapped OCS. As stated above, extending the search to a wider composition space, especially in the direction of the Al is promising, since it could reveal more compositions with PWs at carbon contents even above 0.2 wt pct.

It should be noted that in Figures 6 through 9, the boundary surfaces are not so smooth since they exhibit jagged edges and some irregular sharp points. This behavior is mostly attributed to the rather large discretization step used in mapping procedures, as listed in detail in Table II. A further refinement of the discretization grid should eliminate most of the appearing irregularities, resulting in a continuous and piecewise smooth boundary surface. Yet, the surface might still exhibit some curves, where the derivative normal to the curve and tangent to the surface cannot be defined, *i.e.*, where the curve partitions the surface into two piecewise smooth regions. These curves cannot be eliminated by selecting a smaller step since they originate from an intersection of two or more boundary conditions, which in this case correspond to the alloy design criteria used to define a PW, as listed in Table III. The specific discretization was selected with the notion that issues, like the limited smoothness of boundary surfaces, might occur, however, the increased computational cost associated with a further grid

refinement might not be justifiable since the solution regarding alloy compositions, exhibiting PWs, will not change appreciably.

C. Distribution of Process Window Attributes

Although many alloys exhibit a PW, their characteristics such as the distribution of annealing temperature, fraction of retained austenite, and M_S temperature may vary significantly depending on the composition.

1. Annealing temperature

The distribution of the maximum and minimum annealing temperature of the PWs is shown in Figures 11(a) and (b), respectively. The maximum and minimum temperatures vary from 853 K (580 °C) to 963 K (690 °C) and from 843 K (570 °C) to 953 K (680 °C), with a mode value of 926 K (653 °C) and 914 K (641 °C), respectively. Both distributions are negatively skewed, as the majority of alloys are located in a small region of 913 K (640 °C) to 933 K (660 °C) for the maximum, and a region of 903 K (630 °C) to 923 K (650 °C) for the minimum temperature. Similarly, the reference temperature T_{Ref} in Figure 11(c), follows the same trends as for over 50 pct of the PWs, T_{Ref} lies in the region of 913 K (640 °C) to 953 K (680 °C) and under any circumstances does not exceed 963 K (690 °C). The distribution of the PW range ΔT is shown in Figure 11(d). ΔT does not
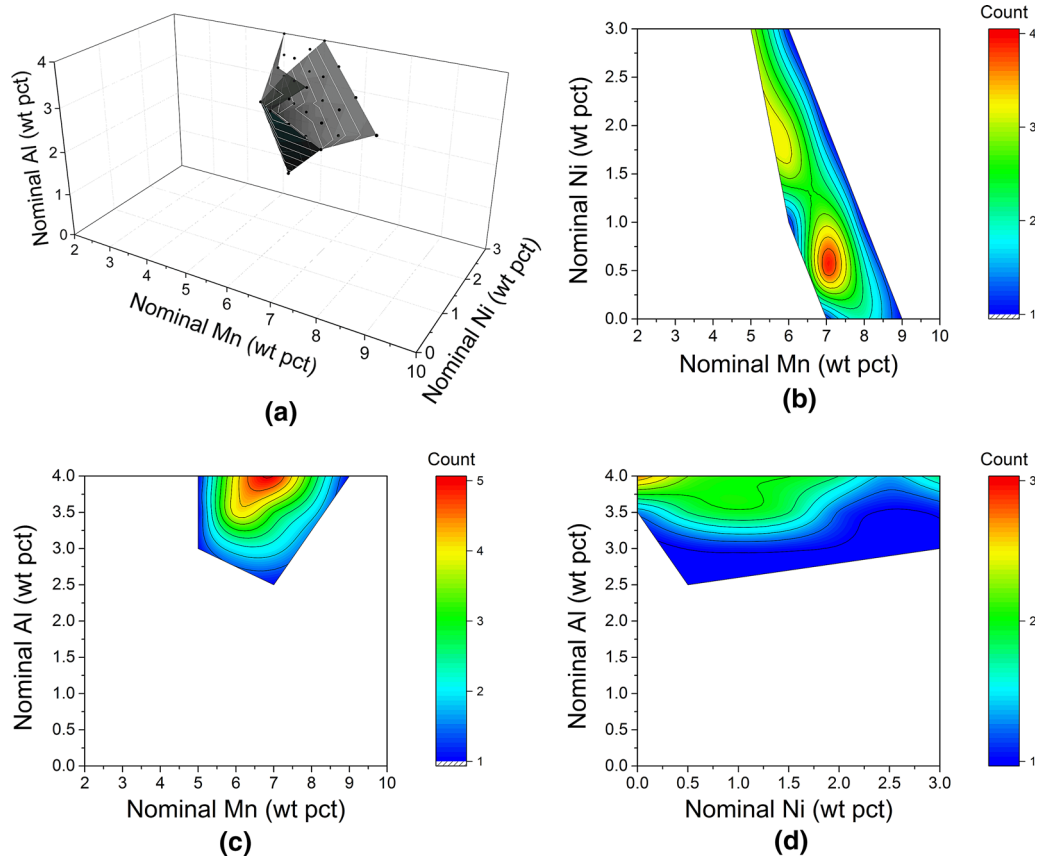
Fig. 9—0.20 Pct C: (*a*) 3D Contour, (*b*) Mn-Ni Projection, (*c*) Mn-Al Projection, and (*d*) Ni-Al Projection.
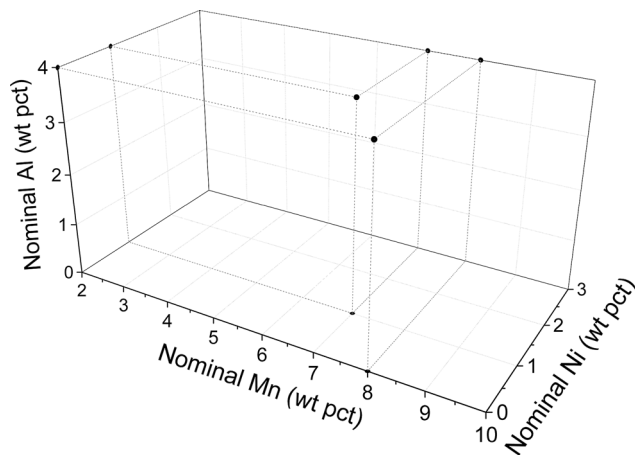

Fig. 10—0.25 Pct C: Only two compositions containing 0.25 wt pct C were found to exhibit a PW.

exceed 20 °C and the distribution is heavily skewed with over 80 pct of the population having a PW range between 10 and 14 °C.

2. Retained austenite

The distribution of maximum and minimum retained austenite fractions found in the PWs are depicted in Figures 12(a) and (b). Both parameters span the entire specified region of 20 to 40 pct, indicating that many PWs are rejected due to the corresponding constraints.

In the case of maximum austenite fraction, the number of PWs increases almost linearly as fractions grow, so the distribution is skewed. A very similar behavior is observed in Figure 12(c), by the retained austenite fraction at the reference temperature T_{Ref}. The trend is discontinued at the minimum $f_{\gamma R}$ as the PWs found decrease significantly when the fraction reaches 38 pct.

3. M_S temperature

The behavior of the M_S temperature is shown in Figure 13. Almost the entire PW population has minimum and maximum M_S values very close to the boundary values specified by the alloy design criteria. The gradient of the M_S with respect to the annealing temperature is steep so a small deviation in annealing temperature, strongly influences the M_S and thus the austenite stability. As a consequence, the PW range (ΔT) is restricted by the constraints set to the M_S temperature. The M_S at the reference temperature T_{Ref} is depicted in Figure 13(c). The distribution ranges between 245 K (−28 °C) and 233 K (−40 °C), with the most common value being approximately 242 K (−31 °C).

D. Effect of Alloying Elements on Process Window Attributes

1. Annealing temperature

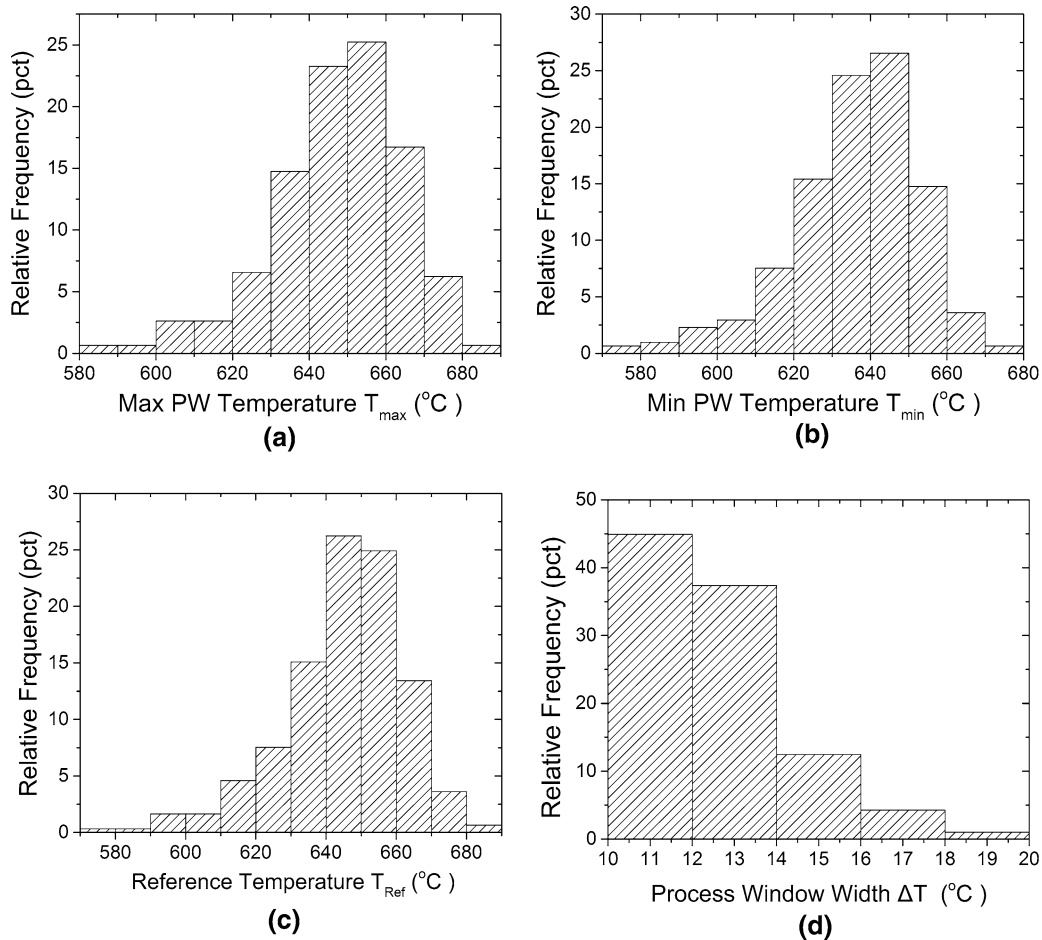The effect of alloying on annealing temperature can be discussed by plotting the reference temperature T_{Ref}

Fig. 11—Distribution of (*a*) Maximum, (*b*) Minimum, (*c*) Reference (T_{Ref}) Temperatures, and (*d*) the Temperature Range ΔT, across the Process Windows.
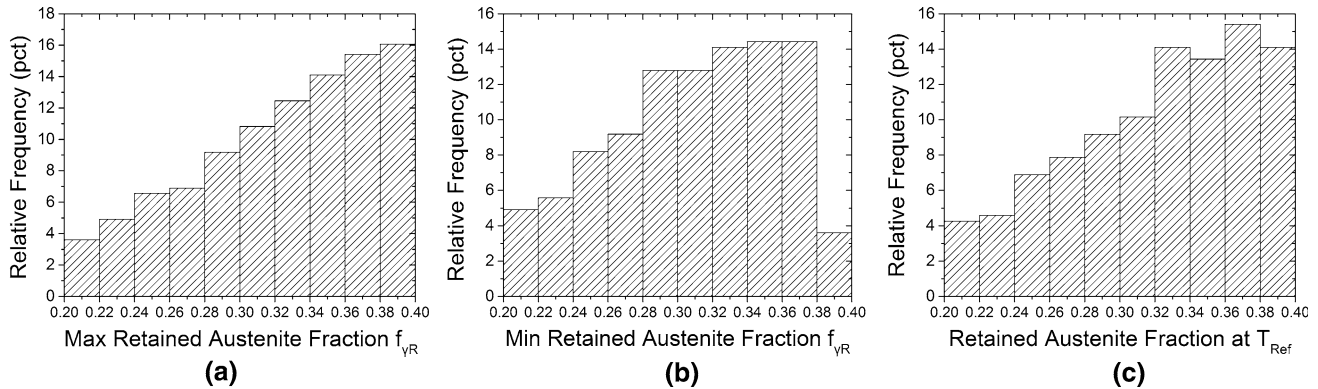

Fig. 12—Distribution of (*a*) Maximum, (*b*) Minimum Retained Austenite volume fractions, and (*c*) the fraction calculated at the Reference Temperature T_{Ref}.

as a function of Mn and Al content. This is depicted in Figures 14(a) through (c) for 0.1, 0.2, and 0.3 pct carbon, respectively. A close observation of the contour surfaces confirms that regardless of C and Ni concentration, the addition of Al raises the annealing temperature in a linear manner. In contrast, increasing the Mn content causes a linear decrease in temperature. The

effect of carbon is similar to that of Al as it shifts the Ni contours to higher temperatures. Unlike Al, excess C inhibits PWs, so as the concentration increases, the surfaces become smaller. It can be seen that as Ni increases, the corresponding surface shrinks. As a consequence, the reference temperature T_{Ref} is reduced with the addition of Ni. An analogous behavior was
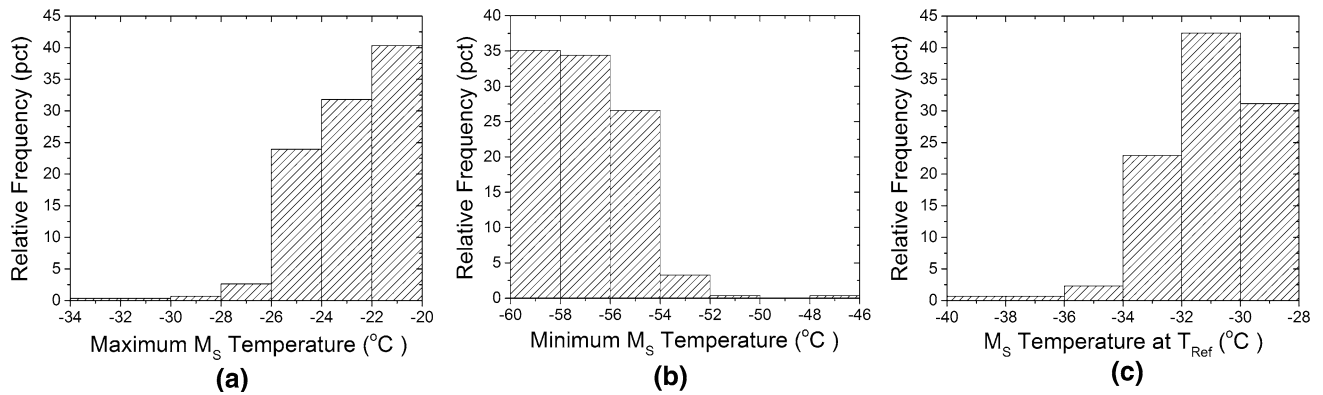
Fig. 13—Distribution of (*a*) Maximum, (*b*) Minimum M_S Temperatures, and (*c*) the M_S calculated at the Reference Temperature T_{Ref}.
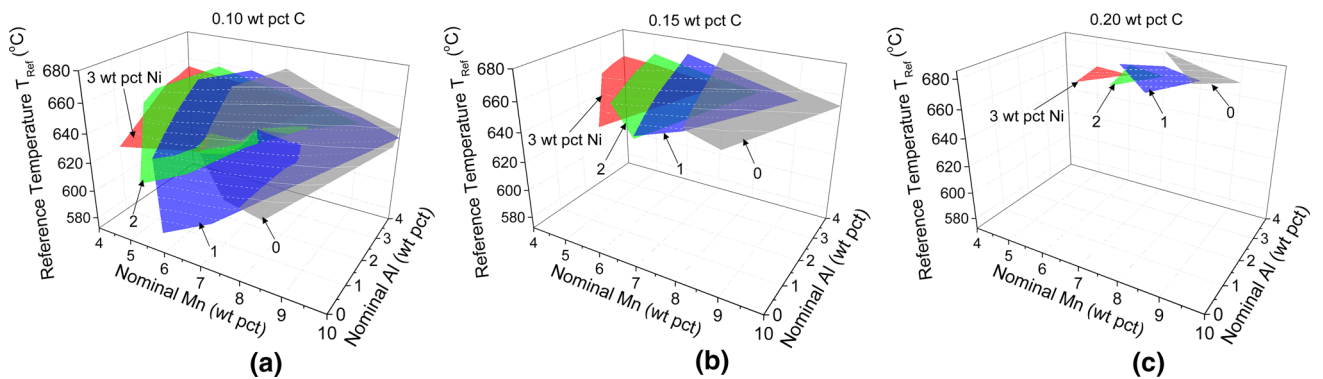

Fig. 14—Reference Temperature T_{Ref} plotted for different Nickel contents at: (*a*) 0.10 pct C; (*b*) 0.15 pct C; and (*c*) 0.20 pct C.
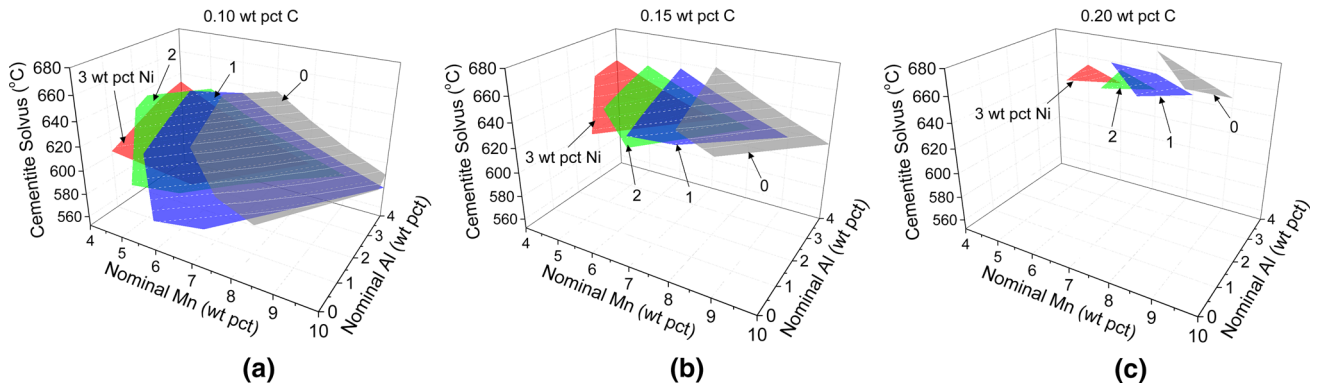

Fig. 15—Cementite Solvus Temperature A_{CM} plotted for different Nickel contents at: (*a*) 0.10 pct C; (*b*) 0.15 pct C; and (*c*) 0.20 pct C.

exhibited by the cementite solvus temperature A_{CM}, which follows in general similar trends, as shown in Figure 15. The increase in A_{CM}, with carbon content, is expected since excess C promotes cementite formation.

2. *Retained austenite*
The fraction of retained austenite calculated at the reference temperature T_{Ref} is depicted as a function of the nominal Mn and Al content in Figures 16(a) through (c) for 0.1, 0.2, and 0.3 pct carbon, respectively. As expected, the addition of C, Mn, and Ni increases the volume fraction of retained austenite. Alloying with Al

has the adverse effect, since it destabilizes austenite. A small amount of Ni can compensate for this behavior and restore the fractions of austenite back to acceptable levels especially in low C-Mn alloys.

3. *M_S temperature*
The M_S temperature fluctuates rapidly over the composition subset found to possess PWs making it impossible to draw solid conclusions. This irrational behavior can partly be explained by the strong gradient of the M_S with respect to annealing temperature inside the PW range, which is apparent in Figure 2.
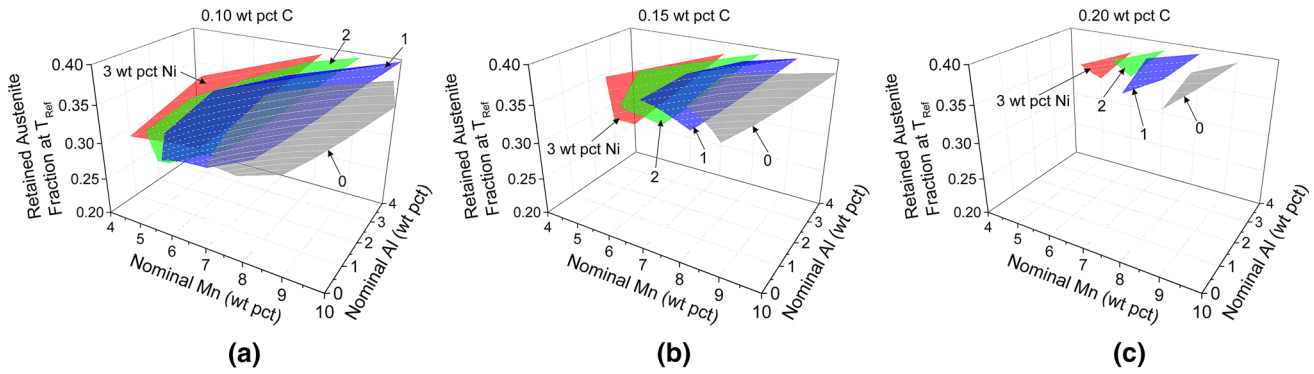
Fig. 16—Retained Austenite volume fraction, calculated at T_{Ref}, plotted for different Nickel contents at: (a) 0.10 pct C; (b) 0.15 pct C; and (c) 0.20 pct C.
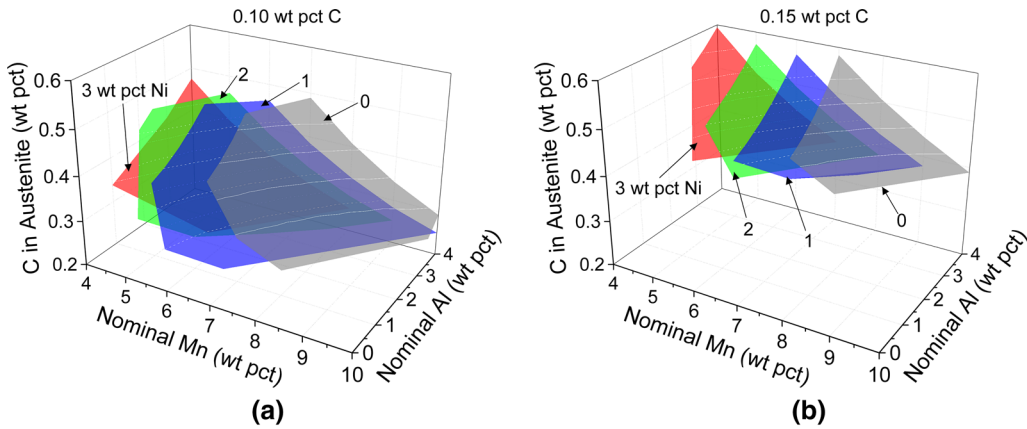

Fig. 17—Carbon concentration in Austenite for different Ni contents at: (a) 0.10 pct C and (b) 0.15 pct C.
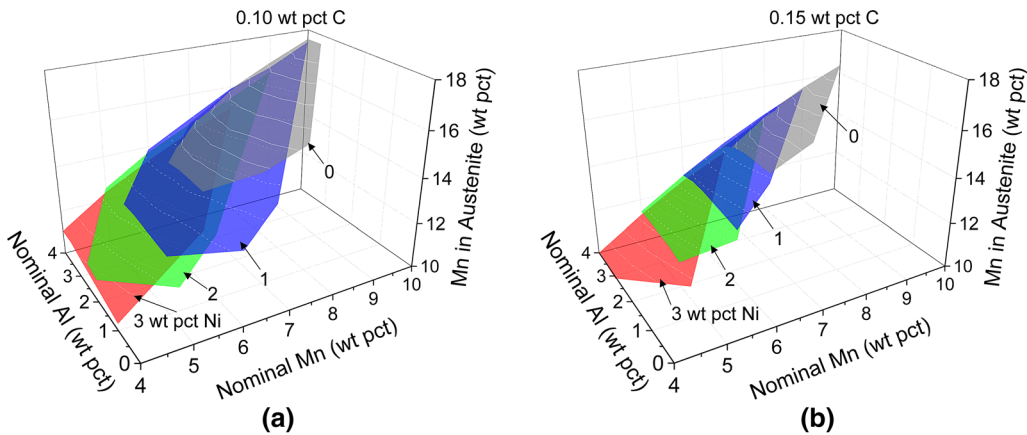

Fig. 18—Manganese concentration in Austenite for different Ni contents at: (a) 0.10 pct C and (b) 0.15 pct C.

4. Austenite composition

The chemical composition of the equilibrium austenite is affected by the nominal alloy composition, as well as the annealing temperature. The austenite composition calculated at the reference temperature T_{Ref}, for alloys that exhibit a PW, is depicted in Figures 17 through 20 for C, Mn, Ni, and Al, respectively. The addition of carbon causes a significant enrichment in C and Al and a depletion of Mn and Ni in austenite. With the addition of Mn, the carbon in austenite decreases, the Mn increases while the Al and Ni concentrations remain unaffected. The addition of Al causes the austenite to become enriched in all alloying elements except Ni, which remains constant regardless of Al and Mn content. Most importantly, a small increase in Al seems to be accompanied by a significant increase of C in austenite. Finally, as the nominal Ni concentration is increased, austenite tends to become enriched in Ni and
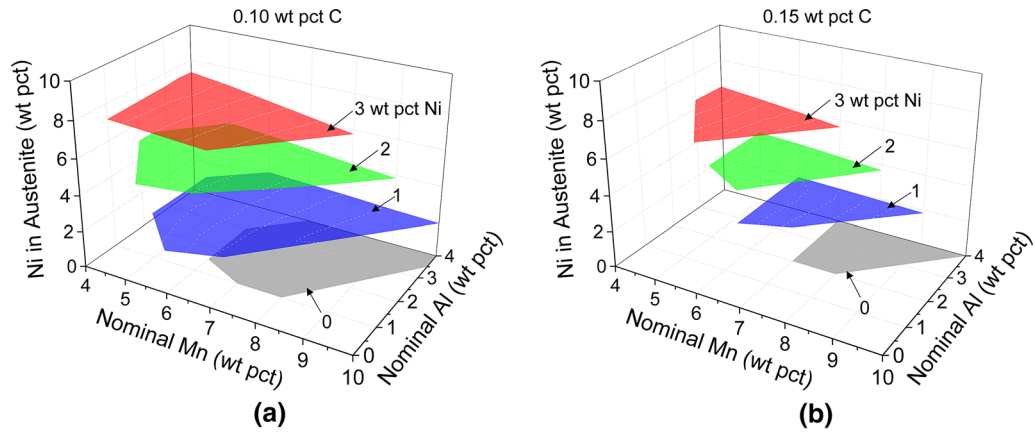
Fig. 19—Nickel concentration in Austenite for different Ni contents at: (*a*) 0.10 pct C and (*b*) 0.15 pct C.
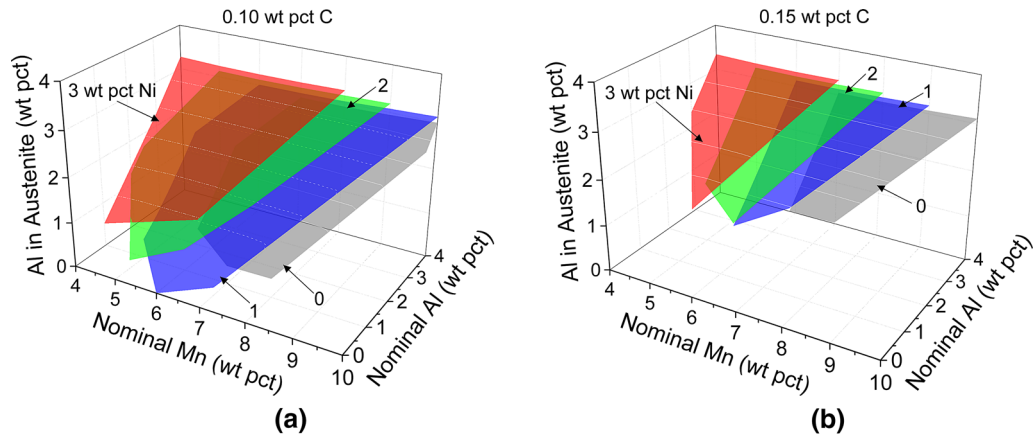

Fig. 20—Aluminum concentration in Austenite for different Ni contents at: (*a*) 0.10 pct C and (*b*) 0.15 pct C.

Table V. The Effect of Alloying Elements on the PW Attributes

Nominal Composition	Reference Temperature T_{Ref}	Cementite Solvus A_{CM}	Retained Austenite Fraction $f_{\gamma R}$	Austenite Composition			
				C	Mn	Ni	Al
↑ C	↑	↑	↑	↑	↓	↓	↑
↑ Mn	↓	↓	↑	↓	↑	—	↑
↑ Ni	↓	↓	↑	↓	↓	↑	↑
↑ Al	↑	↑	↓	↑	↑	—	↑

Al and depleted in C and Mn. The aforementioned observations have been summarized qualitatively in Table V.

Regarding the effect of Aluminum, although it is a ferrite stabilizer it can stabilize austenite indirectly, by allowing the incorporation of more C and Mn in austenite. On the contrary, an excessive addition of Mn and Ni although it increases austenite fractions, could result in reduced stability, since as the Mn content increases the austenite becomes depleted in carbon. As discussed in Reference 28, carbon is a more potent austenite stabilizer compared to Mn, so the addition of extreme amounts of Mn could potentially destabilize austenite. A similar effect could appear in high Ni contents. According to the Andrews equation (Eq. [1]),

the ability of Mn to reduce the M_S temperature is greater than that of Ni. With large Ni additions, the Mn concentration in austenite will decrease and stability might be reduced. It appears that the addition of an austenite stabilizer can, under certain conditions, result in decreased austenite stability in multi-component systems such as the Fe-C-Mn-Ni-Al. In the present study, the effect with respect to Ni is small since it does not exceed 3 pct by weight; however, it is apparent with respect to Mn. Although, as discussed above, even small additions of Ni result in higher amounts of retained austenite. There is a tradeoff between austenite fraction and stability, which highlights the need for a suitable optimization method in order to identify optimized alloy compositions.

Table VI. Top 20 Pareto Optimal Solutions Ranked by Geometric Mean

Ranking	Composition (Wt Pct)	T_{Max} (K (°C))	T_{Min} (K (°C))	T_{Ref} (K (°C))	$f_{\gamma\mathrm{R}}$ (T_{Ref})	M_{S} (T_{Ref}) (K (°C))	$J_{\mathrm{N_1}}$	$J_{\mathrm{N_2}}$	$J_{\mathrm{N_3}}$	$J_{\mathrm{N_4}}$	Geometric Mean
1	0.15C8Mn0Ni2Al	908 (635)	898 (625)	905.5 (632.5)	0.394	236.2 (−36.8)	0.985	0.519	0.768	0.348	0.608
2	0.15C6Mn2Ni1.5Al	908 (635)	898 (625)	905.5 (632.5)	0.388	239.2 (−33.8)	0.951	0.519	0.492	0.535	0.600
3	0.15C8Mn0.5Ni2.5Al	916 (643)	906 (633)	913.5 (640.5)	0.395	236.7 (−36.3)	0.989	0.596	0.718	0.305	0.599
4	0.15C5Mn1.5Ni2.5Al	930 (657)	920 (647)	927.5 (654.5)	0.288	238.9 (−34.1)	0.443	0.731	0.516	0.698	0.584
5	0.10C8Mn1Ni2Al	898 (625)	888 (615)	895.5 (622.5)	0.393	237.9 (−35.1)	0.976	0.423	0.607	0.423	0.571
6	0.20C6Mn1.5Ni3Al	938 (665)	928 (655)	935.5 (662.5)	0.362	240.2 (−32.8)	0.819	0.808	0.405	0.396	0.571
7	0.10C8Mn1.5Ni2.5Al	906 (633)	896 (623)	903.5 (630.5)	0.394	238.6 (−34.4)	0.981	0.500	0.543	0.380	0.564
8	0.15C5Mn2.5Ni3Al	930 (657)	920 (647)	927.5 (654.5)	0.307	240.1 (−32.9)	0.541	0.731	0.409	0.623	0.564
9	0.15C6Mn1.5Ni2Al	918 (645)	908 (635)	915.5 (642.5)	0.354	240.5 (−32.5)	0.779	0.616	0.370	0.556	0.560
10	0.15C7Mn1Ni2Al	914 (641)	904 (631)	911.5 (638.5)	0.386	240.1 (−32.9)	0.941	0.577	0.410	0.436	0.558
11	0.15C6Mn2.5Ni2.5Al	922 (649)	912 (639)	919.5 (646.5)	0.373	240.8 (−32.2)	0.876	0.654	0.347	0.481	0.556
12	0.20C5Mn3Ni3.5Al	936 (663)	926 (653)	933.5 (660.5)	0.349	240.6 (−32.4)	0.754	0.789	0.363	0.441	0.556
13	0.20C6Mn2.5Ni3.5Al	936 (663)	926 (653)	933.5 (660.5)	0.379	240.1 (−32.9)	0.905	0.789	0.411	0.321	0.554
14	0.10C6Mn3Ni1.5Al	900 (627)	890 (617)	897.5 (624.5)	0.382	240.5 (−32.5)	0.920	0.443	0.374	0.610	0.552
15	0.10C5Mn3Ni3Al	920 (647)	910 (637)	917.5 (644.5)	0.282	239.3 (−33.7)	0.412	0.635	0.486	0.730	0.552
16	0.10C5Mn3Ni2Al	910 (637)	900 (627)	907.5 (634.5)	0.313	240.2 (−32.8)	0.572	0.539	0.396	0.752	0.550
17	0.15C6Mn2.5Ni3.5Al	930 (657)	920 (647)	927.5 (654.5)	0.337	240.3 (−32.7)	0.695	0.731	0.388	0.460	0.549
18	0.20C7Mn0.5Ni2.5Al	932 (659)	921.6 (648.6)	929.4 (656.4)	0.392	240.4 (−32.6)	0.971	0.749	0.385	0.318	0.546
19	0.15C4Mn3Ni3Al	930 (657)	920 (647)	927.5 (654.5)	0.276	240 (−33.0)	0.383	0.731	0.419	0.743	0.544
20	0.15C8Mn1Ni3Al	922 (649)	912 (639)	919.5 (646.5)	0.396	239 (−34.0)	0.991	0.654	0.512	0.262	0.543

T_{Max}, T_{Min}, and T_{Ref} are the maximum, minimum, and reference temperatures of the PW, expressed in K (°C). $f_{\gamma\mathrm{R}}(T_{\mathrm{Ref}})$ and $M_{\mathrm{S}}(T_{\mathrm{Ref}})$ are the retained austenite fraction and the M_{S} temperature in K (°C), calculated both at the reference temperature T_{Ref}. $J_{\mathrm{N_1}}$, $J_{\mathrm{N_2}}$, $J_{\mathrm{N_3}}$, and $J_{\mathrm{N_4}}$ are the normalized objectives, which correspond to the austenite fraction, the annealing temperature, the austenite stability, and the composition index, respectively. The four normalized objectives are dimensionless and take values between 0 and 1.

E. Optimization Results: Pareto Optimal Solutions and Ranking of Alloys

By applying the optimization methodology to the identified PWs as described in Sections II–D and II–E, the Pareto optimal solutions were computed using the formal definition and then ranked according to the GM heuristic. From a total of 305 PWs, 173 were identified as Pareto optimal solutions. The top 20 alloys based on the GM heuristic ranking are shown in Table VI. Members of the Pareto optimal set vary in composition as they are scattered across the range of the OCS that exhibits PWs. Nevertheless, almost every solution was found to contain some amount of Ni and Al, highlighting their ability to improve the overall PW behavior. Each Pareto solution combines uniquely the alloy design objectives in an optimal manner, trading off one for the other. In the present study, the top ten alloys according to the GM heuristic ranking, compose a short list which is considered the final optimization result. These alloys perform excellently in all four objectives, resulting in very large GM values. As discussed in Section II–D, the GM heuristic discourages the selection of alloys that perform poorly in one or more objectives, a behavior which is reflected in the selected list, since for these compositions, no single normalized objective vector element ($J_{\mathrm{N_i}}$) takes a value below 0.3. Members of the list contain 0.1 to 0.2 wt pct C, 5 to 8 wt pct Mn, 0 to 2.5 wt pct Ni, and 1.5 to 3 wt pct Al and exhibit a PW of approximately 10 °C wide, with a reference annealing temperature T_{Ref} between 895.5 K (622.5 °C) and 935.5 K (662.5 °C). After intercritical annealing at the corresponding reference temperature, the selected compositions are able to form 29 to 40 pct retained austenite with an M_{S} temperature of 240.5 K (−32.5 °C) to 236.2 K (−36.8 °C), assuming that thermodynamic equilibrium conditions are established. The chemical composition of the selected alloys are in accordance with the recent experimental studies,[3–6,29] which appear to focus in 5 to 7 wt pct containing medium-Mn steels.

The rest of the Pareto optimal solution set attracts some interest as well, since compositions could be selected to suit more specific requirements. For example, compositions like number 16 (0.10C5Mn3Ni2Al) or 19 (0.15C4Mn3Ni3Al), which contain small amounts of carbon and Manganese could be used in applications where weldability is more important. Alloys like number 6 (0.20C6Mn1.5Ni3Al), 12 (0.20C5Mn3Ni3.5Al), and 13 (0.20C6Mn2.5Ni3.5Al), exhibit PWs at relatively elevated temperatures, so they could be selected specifically to allow for accelerated kinetics, and thus to reduce the manufacturing time.

F. Sensitivity Analysis

Since the CI weight vector W_{C} is determined with the aid of the AHP method, it is reasonable that the optimization results might vary for different W_{C} values. To examine the stability of the proposed solution, a sensitivity analysis was performed by systematically evaluating the model for various W_{C} vectors close to the original value of $W_C = [0.259 \quad 0.568 \quad 0.119 \quad 0.054]$. The analysis revealed that the number of Pareto optimal solutions varied slightly as the weight vector changed, however the effect was relatively insignificant.

Additionally, the ranking based on the GM of the objective vector was marginally affected by W_C deviations. More specifically, in the top ten ranked compositions, some reordering occurred, though the members of the list remained for the most part unaltered, an indication that the proposed solution can be considered stable with respect to CI weights.

G. *Implications in Alloy Design*

The alloy design methodology presented above is entirely based on computational alloy thermodynamics. This means that the compositions of ferrite and austenite at intercritical annealing are equilibrium compositions. In addition, the retained austenite fractions and associated M_S temperatures were calculated using these equilibrium compositions. It is anticipated that some of the annealing times in achieving the required austenite fractions and stabilities might be quite long. It is therefore necessary to follow-up this procedure with kinetic simulations concerning the solute partitioning (C, Mn, Al, and Ni) between ferrite and austenite during intercritical annealing of these steels. These calculations will be performed systematically for the short list (top ten) of optimized alloys of Table VI and will provide industrially feasible PWs. Nevertheless, the proposed methodology could be the first step toward the computational alloy design process regarding this class of steels.

IV. CONCLUSIONS

A new alloy design methodology, involving computational alloy thermodynamics and multi-objective optimization, has been presented. The methodology leads to the identification of alloy compositions, which exhibit PWs satisfying specific design objectives and optimized for overall performance. The approach was applied to the design of medium-Mn steels containing Al and/or Ni. The major conclusions of this work are the following:

- Only a fraction of 11 pct (305 out of 2835) of the investigated compositions in the OCS exhibited a PW. The majority of PWs were found for the 0.1 wt pct C content and none was found above 0.25 wt pct C.
- There are clear indications that more PWs exist outside the mapped region and thus an extension of the composition space should be investigated, especially in the direction of Al and Ni.
- A multi-objective optimization method, involving Pareto optimality, was applied to identify a list of optimum alloy compositions, which maximized retained austenite amount and stability, as well as intercritical annealing temperature, while minimized overall alloy content. A heuristic approach was finally employed in order to rank the optimum alloys.
- A short list of optimized alloys ranked according to their overall performance with respect to the design objectives has been determined.

- The proposed approach is based on alloy thermodynamics, and therefore, a follow-up study is necessary to implement kinetic constraints in order to define industrially feasible PWs. However, the method presented here could be the first step in the computational alloy design process.

REFERENCES

1. R.L. Miller: *Metall. Mater. Trans. B*, 1972, vol. 3, pp. 905–12.
2. Z.H. Cai, H. Ding, R.D.K. Misra, and S.Q. Qiguan: *Mater. Sci. Eng. A*, 2016, vol. 652, pp. 205–11.
3. S. Lee and B.C. De Cooman: *Metall. Mater. Trans. A*, 2013, vol. 44, pp. 5018–24.
4. R. Rana, P.J. Gibbs, E. De Moor, J.G. Speer, and D.K. Matlock: *Steel Res. Int.*, 2015, vol. 86, pp. 1139–50.
5. J. Hu, W. Cao, C. Huang, C. Wang, H. Dong, and J. Li: *ISIJ Int.*, 2015, vol. 55, pp. 2229–36.
6. K. Sugimoto, H. Tanino, and J. Kobayashi: *Steel Res. Int.*, 2015, vol. 86, pp. 1151–60.
7. X. Zhao, Y. Shen, L. Qiu, Y. Liu, X. Sun, and L. Zuo: *Materials*, 2014, vol. 7, pp. 7891–7906.
8. Z.H. Cai, H. Ding, X. Xue, J. Jiang, Q.B. Xin, and R.D.K. Misra: *Scripta Mater.*, 2013, vol. 68, pp. 865–68.
9. Z.H. Cai, H. Ding, X. Xue, and Q.B. Xin: *J. Mater. Eng. Perform.*, 2012, vol. 23, pp. 1131–37.
10. A. Grajcar, P. Skrzypczyk, and D. Wozniak: *Arch. Metall. Mater.*, 2014, vol. 59, pp. 1691–97.
11. M. Cai, Z. Li, Q. Chao, and P.D. Hodgson: *Metall. Mater. Trans. A*, 2014, vol. 45, pp. 5624–34.
12. D.W. Suh and S.J. Kim: *Scripta Mater.*, 2016, vol. 126, pp. 63–7.
13. S. Kang, E. De Moor, and J.G. Speer: *Metall. Mater. Trans. A*, 2015, vol. 46, pp. 1005–11.
14. H. Kamoutsi, E. Gioti, G.N. Haidemenopoulos, Z. Cai, and H. Ding: *Metall. Mater. Trans. A*, 2015, vol. 46, pp. 4841–46.
15. P.J. Gibbs, E. De Moor, M.J. Merwin, B. Clausen, J.G. Speer, and D.K. Matlock: *Metall. Mater. Trans. A*, 2011, vol. 42, pp. 3691–3702.
16. H.L. Lukas, S.G. Fries, and B. Sundman: *Computational Thermodynamics the Calphad Method*, 1st ed., Cambridge University Press, Cambridge, 2007.
17. J.O. Andersson, T. Helander, L. Höglund, P. Shi, and B. Sundman: *Calphad*, 2002, vol. 26, pp. 273–312.
18. K. Andrews: *J. Iron Steel Inst.*, 1965, vol. 203, pp. 721–27.
19. D. Koistinen and R. Marburger: *Acta Metall.*, 1959, vol. 7, pp. 59–60.
20. Y. Censor: *Appl. Math. Optim.*, 1977, vol. 4, pp. 41–59.
21. O. Grodzevich and O. Romanko: *Proc. First Fields-MITACS Ind. Probl. Workshop*, Toronto, Canada, 2006, pp. 89–101.
22. W. Jakob and C. Blume: *Algorithms*, 2014, vol. 7, pp. 166–85.
23. I.Y. Kim and O.L. de Weck: *Struct. Multidiscip. Optim.*, 2006, vol. 31, pp. 105–16.
24. R.W. Saaty: *Math. Model.*, 1987, vol. 9, pp. 161–76.

25. H.A. Taha: *Operations Research: An Introduction*, 8th ed., Pearson, Upper Sadle River, NJ, 2007, pp. 490–500.
26. T.L. Saaty: *Int. J. Serv. Sci.*, 2008, vol. 1, pp. 83–98.
27. H. Huang, O. Matsumura, and T. Furukawa: *Mater. Sci. Technol.*, 1994, vol. 10, pp. 621–26.
28. E. Gioti, H. Kamoutsi, and G.N. Haidemenopoulos: *Proc. 2nd Int. Conf. High Manganese Steel*, Aachen, Germany, 2014, pp. 337–40.
29. S. Chen, Y. Bao, H. Dong, and W. Cao: *Adv. Mater. Res.*, 2014, vol. 1063, pp. 3–6.